10

Atomic Scale Study of Deformation and Failure Mechanisms in Ceramic-Reinforced Metal-Matrix Composites

Avinash M. Dongare[1] Bruce LaMattina[2]
[1]*Materials Science and Engineering, North Carolina State University, USA*
[2]*Rutgers, The State University of New Jersey*
USA

1. Introduction

One of the long-standing problems in materials research has been the development and improvement of materials capable of withstanding ballistic/blast impact. These materials, often referred to as blast and penetration resistant materials (BPRMs), require the ability to mitigate damage and dissipate energy and momentum. These materials are designed to stop fragments and/or projectiles while preventing behind armor debris or spall. Functionally graded ceramic particle reinforced metal-matrix composites (MMCs) are an emerging class of materials that show significant promise for applications in protective structures due to their improved damage mitigation response in addition to their superior strength, stiffness and wear resistance. The improved damage mitigation is attributed to the compositional/structural gradients introduced through the variation of the concentration of the reinforcing ceramic particles (SiC, Al_2O_3, etc.) in the matrix [Mortensen & Suresh, 1995; Suresh & Mortensen,1997]. These functionally graded materials show promise to reduce the need for layered structures that are susceptible to delamination and the formation of axial cracks initiated at the interface of the ceramic and the more ductile backing material. The mechanisms responsible for plastic deformation and failure of these metal-matrix composites, however, are complex and are affected by multiple factors, such as the distribution and location/size of the reinforcing particles, grain size in the metal-matrix, the structural characteristics of the interface between the particles and matrix grains, and loading conditions [Li at Ramesh, 1998, Li et al.,2007]. The design and optimization of BPRM nanocomposite materials can be significantly accelerated by improvements in the understanding of the deformation and failure mechanisms under conditions of ballistic impact. An optimized design of these materials, therefore, requires a fundamental understanding of the links between the length scales (particle size/distribution, layer thickness) and properties (structure, chemistry, etc.) of these composites that enable enabling a combination of high strength and good ductility, and improved failure resistance in impact environments.

While there has been significant progress toward understanding the behavior of these materials, there are still major knowledge gaps to be filled with respect to the identification and characterization of the elementary processes responsible for plastic deformation and failure. **These knowledge gaps are attributed to the inability to fully integrate theory, models, and**

experiments because of disparate time scales and the heterogeneous nature of these materials. The time scales of the processes in these experiments can range from picoseconds to micro-seconds and the length scales can range from nanometers to micrometers [Remington et al., 2004]. These small time scales of the processes make it difficult to identify and characterize the elementary processes responsible for plastic deformation and failure using experiments alone. The molecular dynamics (MD) simulation technique has the ability to provide the atomic level structural information on the relevant micromechanisms at the time-scales of the spall experiments and may be instrumental in physical interpretation of experimental observations [Dongare et al, 2010a]. The applicability of MD simulations as an analysis/ predictive tool, however, relies on the accuracy of the interatomic potentials to model the interactions between atoms in the system. The complex heterogeneity arises from the multi-component interactions that results in complex bonding characteristics at the metal-ceramic interfaces. This heterogeniety limits the applicability of the MD technique due to inavailability of interatomic potentials capable of providing an accurate description of the structural and energy characteristics of metal-ceramic interfaces at the atomic scale. A new class of interatomic potentials referred as the angular dependent Embedded Atom Method (A-EAM) [Dongare et al, 2009a;Dongare et al, 2009b] has been recently developed that extends the ability of MD simulations to MMCs by combining the potentials conventionally used for metals with those conventionally used for ceramics in one functional form.

This chapter provides an overview of the current availability of interatomic potentials to investigate deformation and failure behavior in metal-matrix composites at the atomic scales using MD simulations in Section 2. An in-depth discussion on the formulation of interatomic potentials for complex metal-ceramic interactions is also provided in Section 3 and an example parameterization is provided in Section 4. The applicabilty the A-EAM is demonstrated by investigating the strengthening and failure behavior of Si-particle reinforced Al-matrix nanocrystalline composites at high strain rates in Section 5.

2. Interatomic potentials for Molecular Dynamics Simulations

The MD simulations study the evolution of the system as a function of time using classical atomistic models defined as interatomic potentials [Allen & Tildesley (1987)]. The interatomic potentials, $U(\vec{r}_1,\vec{r}_2,...,\vec{r}_N)$, describe the dependence of the potential energy of a system of N atoms as a function of the positions $\vec{r}_i$ of the atoms. The Born-Oppenheimer approximation states that the electrons adjust to the changing atomic positions since they move much faster than atomic nuclei. This allows the exclusion of interactions for electrons in interatomic potentials and the potential energy can be defined based on atomic positions. Thus, to run a MD simulation, only the details of the interatomic interactions need to be specified in addition to the initial coordinates of the atoms in the system and boundary conditions. This is an important advantage that enables MD simulations to be treated as computer experiments and are therefore capable of discovering new physical phenomena or processes like real experiments. In addition, the analysis of the results provides complete information of the phenomena of interest at atomic-scale resolution. This predictive power of the MD method, however, is limited by the high computational cost of the simulations, that leads to the severe limitations on time and length scales accessible for the simulation. While the current state-of-art MD simulations boast up to 10^{12} atoms (~ 10 micron size cubic samples) using hundreds of thousands of processors on one of the world-largest supercomputers [Germann & Kadau, 2008], the duration of most of the simulations in the area of materials research do not exceed tens of

nanoseconds. The length-scales and the time scales of the MD simulations is largely defined by the computational efficiency of the interatomic potentials used to define the interatomic interactions.

The interatomic potentials typically are analytical functions that define the energy of an atom based on the coordinates of its neighboring atoms. The parameters of the analytical functions are chosen to describe properties of the material system as observed experimentally (crystal structure, cohesive energy, density, elastic constants, phase transformations, etc.) or as predicted using *ab initio* simulations where experimental data is not available. Metals and metallic alloys have been studied using the Embedded Atom Method (EAM) [Daw & Baskes, 1984; Foiles, 1985; Johnson, 1988] potentials, whereas covalently bonded systems have been studied using the Stillinger – Weber (SW) potential [Stillinger & Weber, 1985; Ding & Anderson, 1986] for Si and Ge, Tersoff (TF) potential [Tersoff, 1988a, 1988b] for Si and C, and the Brenner potential [Brenner, 1990] for hydrocarbon systems. Each of these potentials has a unique functional form and underlying physical concept that allows them to model distinguishing characteristics of the material system. For example, the EAM potential uses an embedding energy term that simulates the effect of an atom embedded in an electron density in metals. The SW potential uses an explicit angular term that stabilizes the diamond cubic lattice for Si and Ge. The TF potential uses a bond order interaction (which includes an angular dependence) that defines the strength of a bond based on the surrounding environment for Si, Ge, and C. These unique functional forms and concepts limit the transferability of these potentials from metallic systems to covalent systems and vice versa and hence limit the atomistic studies to pure systems or alloys with similar bonding characteristics. The Modified Embedded Atom Method (MEAM) potential [Baskes, 1992] is an attractive potential to model mixed metal-covalent systems as it includes parameterization for many cubic metals, as well as Si, Ge, C, H, N, and O. However, the formulation uses a many-body angular screening function as a cutoff mechanism that makes the potential computationally expensive. In addition, the parameterization of the mixed cross interactions in mixed systems also requires an adjustment of the parameters of the pure components [Thijsse, 2005] that will require testing the performance of the potentials for the pure systems.

The applicability of MD simulations to investigate deformation and failure micromechanisms in ceramic particle-reinforced MMCs requires the development of new computationally efficient interatomic potenials that are able to accurately reproduce the structural and energy characteristics of the metal matrix, the ceramic phase, as well as the metal-ceramic interface. An easier solution would be to design new alloy potentials by combining the well-established and thoroughly tested potentials developed for pure components within a unified approach. A number of studies have focused on the relationships between various potentials to justify this unified approach. For example, a potential for the Pt-C system was developed with an analytical form that reduces to the bond-order Brenner potential for C and an EAM-like potential for Pt [Albe et al., 2002]. Similar connections between the EAM formalisms and the bond-order scheme of the TF potential [Brenner, 1989] and between the SW and MEAM potentials [Thijsse, 2002] have been discussed. These studies suggest that despite the apparent distinctions between the functional forms and underlying physical arguments used in the description of interatomic bonding in metallic and covalent systems, a unified approach is feasible.

This chapter discusses the idea of developing a unified interatomic potential for systems with mixed type of bonding is extended to combine the EAM potential for metals with the SW potential commonly used in simulations of Si [Dongare et al, 2009a] and the TF potential

for Si and C [Dongare et al, 2009b]. The combined Angular-dependent EAM (A-EAM) potential incorporates a description of the angular dependence of the interatomic interactions into the framework of the EAM potential to make it compatible with the SW/TF potentials. The A-EAM potential retains all the properties of the pure components as predicted by the original SW/TF and EAM potentials and therefore eliminates the need for extensive testing for pure systems. In addition, the scope of the potential parameterization is limited to cross-interaction between the components. An example of the parameterization of the cross-interaction in the A-EAM potential is given for the Al-Si system here to study the micromechanisms related to deformation and failure of functionally graded Si reinforced Al-matrix composites (A359 alloy). Experimentally, the as-cast Al-Si (A359) alloy consists of a dendritic microstructure containing fine Si particles (wt % ~ 9 % Si) [Li et al.,1998, 2007]. The EAM potential for Al in the form suggested in Ref. [Mishin et al., 1999] is chosen as it provides a good description of the unstable and stable stacking fault energies and the surface and grain boundary energies in Al. In addition, the advantage of this potential is in the simplicity of the functional form and the availability of parameterizations for many metals, allowing for an easy implementation for a broad range of alloy systems. For pure Si, the original parameterization of SW potential [Stillinger & Weber, 1985] is used as it has been found to provide a good description of the crystalline, liquid , and amorphous phases of Si. The choice of the EAM and SW potentials renders the A-EAM potential to be computationally efficient and also provides an accurate description of the pure systems. The functional formulation of the A-EAM potential and the parameterization for the Al/Si cross-interactions are described in Section 3 below.

3. The Angular-dependent Embedded Atom Method (A-EAM)

A unified alloy potential based on a reformulation of the EAM and SW potentials in a compatible functional form [Dongare et al, 2009a] is discussed in this section. A reformulation of the conventional EAM potential into a form that includes three-body terms in the expression for the total electron density function is presented first, followed by the description of an approach for incorporation of the angular dependence compatible with the SW potential.

3.1 Reformulation of the EAM potential

The energy of an atom in the EAM formulation [Daw & Baskes, 1984; Foiles, 1985; Johnson, 1988], the energy of an atom is expressed as

$$E_i = \frac{1}{2}\sum_{j \neq i} V_{ij}(r_{ij}) + G_i[\rho_i] \quad (1)$$

where, $V_{ij}(r_{ij})$ and $f_j(r_{ij})$ are the pair energy contribution for atom i due to interactions with neighboring atoms j separated by a distance r_{ij}, and G_t is the "embedding energy" of an atom i that is dependent on the 'electron density'around atom i. The distributions of neighboring atoms j determines the electron density ρ_i for atom i, and is calculated based on individual electron density contributions, $g_j(r_{ij})$, from neighboring j atoms and the separation distance r_{ij}, as$\rho_i = \sum_{j \neq i} g_j(r_{ij})$

As discussed in [Dongare et al, 2009a] and [Dongare et al, 2009b], the ability to combine the EAM potentials with the SW or the TF potentials requires the addition of an angular dependence to the electron density. This chapter provides a more efficient formulation of the equations in [Dongare et al, 2009a]. The electron density term no longer requires a square-root

dependence. Instead, the electron density for an atom in the A-EAM formulation is written as

$$\rho_i = \sum_{j \neq i} g_j(r_{ij}) + g_i^0 \sum_{k \neq i} \sum_{j \neq i} g_j(r_{ij}) g_k(r_{ik})\, g_\theta(\theta_{jik}) \tag{2}$$

For modeling pure metals, the parameter, g_0, is set to 0. The angular contribution on the right consists of a product of the partial electron density contributions and the bond angle only for unique triplets of atoms *(i, j, k)* [Thijsse, 2002] and is included using a parameter g_0. Formulations of this type for the electron density can be used to combine EAM potentials for metals with angular-dependent potentials for covalenty bonded materials. The modeling of Si/Ge systems with metals requires either reformulating the SW potential [Dongare et al, 2009a] or the Tersoff potential [Dongare et al, 2009b] as discussed below.

3.2 Reformulation of the SW potential

The SW formation for the energy of an [Stillinger & Weber, 1985] is given by

$$V_i = \frac{1}{2} \sum_{j \neq i} V_{ij}(r_{ij}) + \sum_{j,k \subset T_i} V_{jik}(\vec{r}_i, \vec{r}_j, \vec{r}_k) \tag{3}$$

The two-body ($V_{ij}(r_{ij})$) energy term is similar to the two-body term in the EAM formulation and has a shorter cutoff for the covalent interaction. The three-body (V_{jik}) term defines the energy due to an angle between two bonds and only accounts for unique triplets as

$$V_{jik}(\vec{r}_i, \vec{r}_j, \vec{r}_k) = \lambda \exp\left[\frac{\gamma\sigma}{r_{ij} - r_c} + \frac{\gamma\sigma}{r_{ik} - r_c}\right] (\cos\theta_{jik} + 1/3)^2 \text{ for } \mathrm{r_{ij}} < \mathrm{r_c}, \mathrm{r_{ik}} < \mathrm{r_c} \tag{4}$$

(8)

Here, θ_{jik} is an angle between bonds ij and ik. This three-body can be considered as a formulation of the embedding energy used in the EAM potential [Dongare et al, 2009a]. As mentioned earlier, the electron density term however no longer requires a square-root dependence The embedding energy is simply written as the three body term

$$G_i(\rho_i) = \sum_{j,k \subset T_i} V_{jik}(\vec{r}_i, \vec{r}_j, \vec{r}_k) = g_i^0 \sum_{j,k \subset T_i} g_{ij}(r_{ij}) g_{ik}(r_{ik}) (\cos\theta_{jik} + 1/3)^2 \tag{5}$$

Here, theterms $g_{ij}(r_{ij})$ and $g_{ik}(r_{ik})$ can be considered as partial electron density terms written as

$$g_{ij}(r_{ij}) = g_e^{Si} \exp\left(\frac{\gamma\sigma}{r_{ij} - r_c}\right) \tag{6}$$

Here, the parameter g_e^{Si} is adjustable and used only to scale the electron density contributions when considering cross-interactions and is normalized to 1 by setting $g_i^0 = \frac{\lambda}{(g_e^{Si})^2}$. The partial electron density contributions in this formulation are defined for a type of bond(*ij* or *ik* being metallic, covalent, or metal-covalent) and not only by the type of the neighboring atom *j*. This formulation also allows for the incorporation of charge transfer effects between species wherein $g_{ij}(r_{ij}) \neq g_{ji}(r_{ij})$ [Dongare et al., 2009a]. Such effects prove to important to capture the predicted properties of experimental data and *ab initio* calculations.

3.3 Angular-dependent EAM compatible with SW potential

The A-EAM formulation [Dongare et al, 2009a] that combines both the EAM and SW formulations is given by:

$$E_i = \frac{1}{2}\sum_{j\neq i} V_{ij}(r_{ij}) + G_i[\rho_i] \tag{7}$$

Here the embedding energy, G_i , is written as a function of the electron density ρ_i which is summation of partial electron density contributions from a two-body and a three-body interactions. As mentioned, the electron density term is simply a summation of the pair terms and three-body terms ad no longer requires a square-root dependence The embedding energy is simply written as the three body term. This elimination of the square root term used in [Dongare et al, 2009a] that reduces the computational costs for the combined potential. The combined electron denstity term is written as

$$\rho_i = g_i^{\emptyset}\sum_{j\neq i} g_{ij}(r_{ij}) + g_i^{\theta}\sum_{k\neq i}\sum_{j\neq i} g_{ij}(r_{ij})g_{ik}(r_{ik})\,(cos\,\theta_{jik} + 1/3)^2 \tag{8}$$

The parameter, $g_i^{\emptyset}$ is set to be equal to 1 for the metal atom and equal to 0 for the covalent atom. The parameter g_i^{θ} is set to be equal to 0 for the metal atom and to $g_i^{\theta} = \frac{\lambda}{(g_e^{Si})^2}$. These parameters ensure that the combined electron density given by Eq. (8) reduces to the electron density function for the metal atom given by the EAM potential, and to the three-body term for the covalent atom given by the SW potential for pure Si. The combined potential that reduces to the conventional SW and EAM potentials for pure components can be then formulated as:

$$E_i = \frac{1}{2}\sum_{j\neq i} V_{ij}(r_{ij}) + G_i\left[g_i^{\emptyset}\sum_{j\neq i} g_{ij}(r_{ij}) + g_i^{\theta}\sum_{k\neq i}\sum_{j\neq i} g_{ij}(r_{ij})g_{ik}(r_{ik})\,(cos\,\theta_{jik} + 1/3)^2\right] \tag{9}$$

Here, the form of the two-body term $V_{ij}(r_{ij})$ is taken as the pair-energy terms for the EAM potential for the metal atom and the SW potential for the covalent atom. Due to the explicit angular dependence in the electron density function given by Eqs. (9), this potential is referred to as the angular-dependent embedded atom method (A-EAM) potential.

4. A-EAM Potential for Si-particle reinforced Al-matrix composites

The A-EAM formulation given by equation (9) enables the modeling of metal-covalent interactions in alloys wherein the energy of an Al atom due to a neighboring Si atom is modified by only the pair term in the electron density fuction and a pair energy term for the Al-Si cross-interaction. Similarly, the energy of a Si atom due to a neighboring Al atom is modified by only through the angular term in the electron density function for the Si atom and the pair energy term for the Al-Si cross-interaction. The capability of the A-EAM potential is demonstrated using an example parameterization of the Al/Si system below.

The pair energy term and the partial electron density contribution for the Al-Si cross-interactions is chosen as:

$$V_{ij}(r_{ij}) = A_{ij}\,exp\left[-\alpha_{ij}\left(\frac{R_M}{r_{ij}-R_M}\right)\right]\left(\frac{r_{ij}}{\sigma_{ij}}\right)^{-p} - B_{ij}\,exp\left[-\beta_{ij}\left(\frac{R_M}{r_{ij}-R_M}\right)\right]\left(\frac{r_{ij}}{\sigma_{ij}}\right)^{-q} \tag{10}$$

$$g_{ij}^{Al-Si}(r_{ij}) = g_{ji}^{Si-Al}(r_{ij}) = g_e^{Al-Si}\,exp\left\{-\gamma_{ij}^{Al-Si}\left(\frac{R_M}{r_{ij}-R_M}\right)\right\} \tag{11}$$

where $A_{ij}, B_{ij}, \alpha_{ij}, \beta_{ij}, \sigma_{ij}, R_M, p, q, g_e^{Al-Si}$, and γ_{ij}^{Al-Si} are fitting parameters used to reproduce the structural energetics of the various Al/Si phases as predicted using DFT calculations. It should be noted that the partial electron density contributions $f_{ij}(r_{ij})$ are defined based on type of bond i.e. Si-Si, Al-Al, and Al-Si. The functional form for the partial electron density attributed to an Al-Si bond is given by

Since there are no stable AlSi alloys (in the solid phase) observed experimentally, the parameters for the electron density function and the pair energy function for Al-Si cross-interactions, given by Eqs. (10)-(11), are selected based on the results of DFT calculations performed for several representative Al-Si bulk alloy structures. Since the number of the energy and structural parameters evaluated in DFT calculations exceeds the number of the fitting parameters, the fitting procedure is not aimed at reproducing the exact values of the material properties predicted in the DFT calculations. Rather, the results of the DFT calculations and the experimental data on the enthalpy of mixing of liquid Al-Si solutions [Kanibolotsky et al., 2002] are considered together as a target in the optimization of the overall agreement. Although several sets of parameters were obtained that provided a good agreement (less than 10 % deviation) with DFT results, the prediction of the enthalpy of mixing of the liquid alloy was the true test to study material behavior in extreme environments (high temperatures, pressures, and strain rates). The final parameter set chosen was found to provide an overall satisfactory description of the DFT results in addition to excellent prediction of the mixing behavior of the liquid alloy.

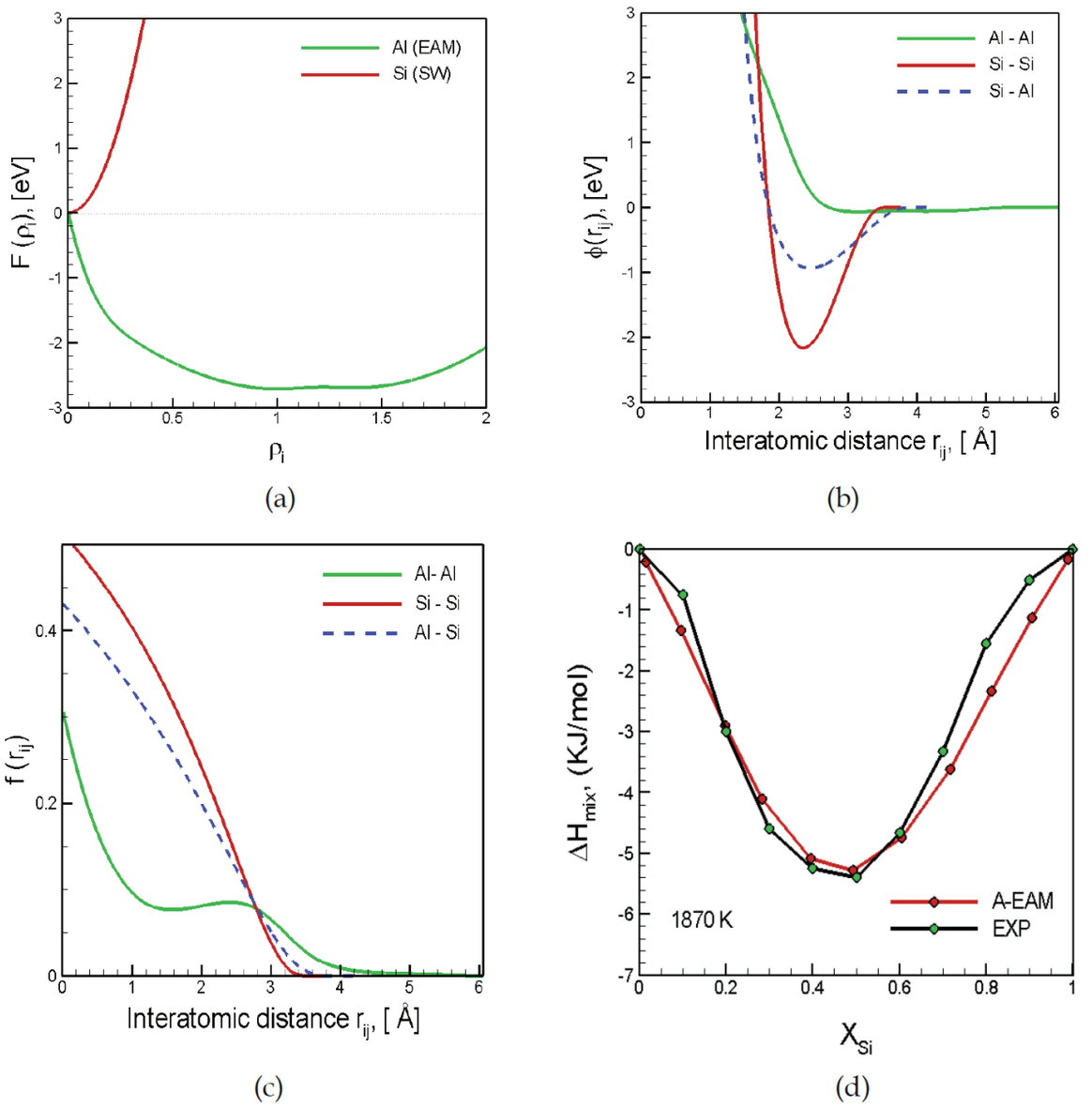

Fig. 1. Plots of the (a) embedding energy functions, (b) pair energy functions, and (c) partial electron density contributions for EAM Al (green line) and SW Si (red line) in the A-EAM formulation. The fitting of the cross-interactions is limited to the Al-Si pair energy and the Al-Si partial electron

density contributions (dashed blue line) in (b) and (c), respectively. The enthalpy of mixing of liquid Al-Si alloy at 1870 K as predicted by the A-EAM potential (red line) is shown in (d) in comparison to experimental data [Kanibolotsky et al., 2002] (black line).

The plots of the embedding energy, the pair energy, and the partial electron density for Si (red lines) and Al (green lines) are shown in Fig. 1.(a), (b), and (c) respectively. The plots of the the pair energy functions and the partial electron density functions and are shown by the dashed blue lines in Fig. 1.(b), and (c), respectively. Thus, according to Eq. (2) and the plots in Fig. 1., the presence of Al atoms in the neighborhood of a Si atom causes a reduction in the partial electron density at the location of a Si atom and a reduced pair energy and therefore results in the weakening of the strength of the Si-Si interactions. This weakening increases the tolerance of the local configuration in Si to deviations from the perfect diamond lattice structure in the presence of Al atoms. This observation is consistent with the results of recent DFT calculations which show a weakening of the Si-Si bonds at Al/Si interface [Nakayama et al., 2006]. The prediction of the experimental dependence of the enthalpy of mixing for the liquid Al-Si alloy at 1870 K by the A-EAM potential is shown in Fig. 1.(d) in comparison to that obtained using experiments [Kanibolotsky et al., 2002]. The plot shows excellent agreement of the predication using the A-EAM potential that shows a minimum of -5.36 kJ/mol at a concentration of 49 at. % Si with experimental data exhibiting a minimum of -5.4 kJ/mol at a composition of 50 at. % Si. The accurate prediction of the mixing behavior across the composition range and the overall prediction of structural characteristics and energetics from DFT calculations enables the A-EAM to predict the relevant intermixing/melting behavior at Al/Si interfaces in extreme environments such as shock loading and radiation damage. More details of the fitting procedure and a quantitative analysis of the performance of the A-EAM potential in comparison to DFT calculations is provided elsewhere [Dongare et al., 2011].

5. Deformation and Failure Behavior of MMCs at High Strain Rates

MD simulations with the newly developed A-EAM Al/Si potential are used to investigate the strengthening and failure behavior of functionally graded Al/Si composites. Experimentally, the as-cast Al-Si (A359) alloy consists of a dendritic microstructure containing fine Si particles (wt % ~ 9 % Si) [Li et al, 2007]. While it is beyond the capabilities of MD simulations to model length scales that incorporate the gradation in composition as observed experimentally, the response of the material at local regions with different compositions can be investigated individually using MD simulations. Nanocrystalline Al/Si systems with varying volume fractions of Si grains are used as the first approximations of the local microstructure in the functionally graded Al/Si alloy. The initial Al/Si nanocrystalline systems with an average grain size of 6 nm and containing 43 grains are created using the Voronoi construction method [Derlet & Van Swygenhoven 2003]. The distribution of the Si grains is chosen at random with random grain orientations depending on the desired composition of the nanocomposites. To study the effect of volume fraction, five Al/Si nanocrystalline systems are created with volume fractions of ~ 5 %, ~ 16 %, ~ 28 %, ~ 35 %, and ~40% Si. The volume fraction is defined as the percentage of Si grains in the nanocrystalline Al/Si system. To facilitate easy comparison, the nanocrystalline composites of different compositions are created with the same grain morphologies and the same grain orientations. Periodic boundary conditions are used in all the three directions. The as-created systems are first relaxed to have zero pressure, and then equilibrated at 300 K for 100 ps. The elements of the atomic-level stress tensor are calculated as

$$\sigma_{\alpha\beta}(i) = -\frac{1}{\Omega_0}\left[\frac{1}{2}\sum_j F_{ij}^{\alpha} r_{ij}^{\beta} + M_i v_i^{\alpha} v_i^{\beta}\right] \tag{15}$$

$$\sigma_m = (\sigma_x + \sigma_y + \sigma_z)/3 \tag{16}$$

where σ_x, σ_y, and σ_z are the stresses averaged over the entire system in the X, Y, and Z directions, respectively.

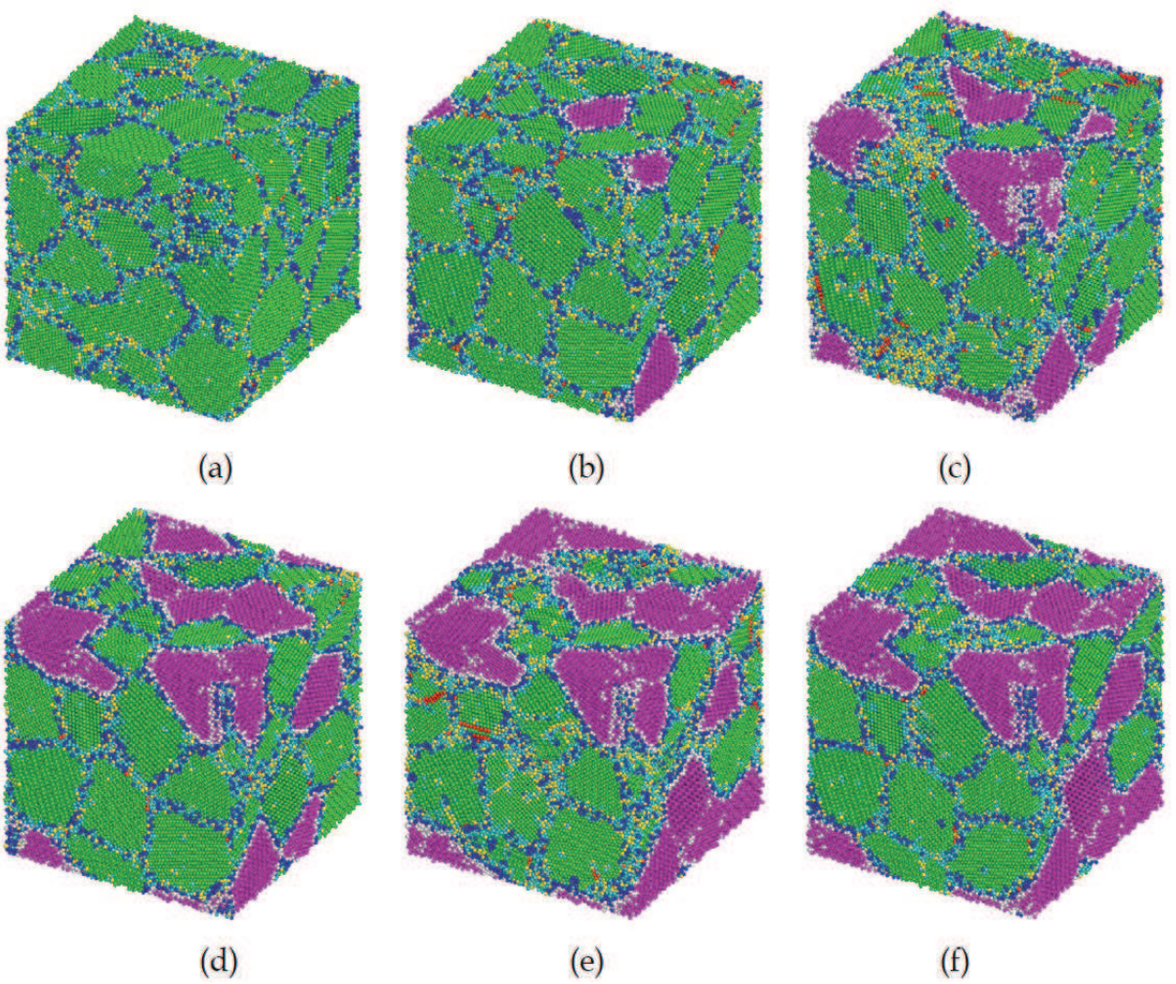

Fig. 2. The initial configuration of nanocrystalline Al/Si systems with an average grain size of 6 nm and a total of 43 grains and each atom is colored according to the CNA/CN values. The compositions (volume fractions) are : (a) pure Al, (b) ~ 5 % Si, (c) ~ 16 % Si, (d) ~ 28 % Si, (e) ~ 35 % Si and (f) ~ 40 % Si.

The common neighbor analysis (CNA) [Honneycutt & Andersen , 1987] in addition to coordination number (CN) is used to identify local deformations in the FCC and diamond-cubic lattice. The initial nanocrystalline Al/Si systems with an average grain size of 6 nm are shown in Fig. 2. with the atoms colored according to the CNA/CN values. The contour for the Al atoms colored according to the CNA/CN characterization is as follows: the green atoms represent bulk fcc stacking, the red colored atoms represent local hexagonal close-packed order (stacking faults), the yellow atoms represent a coordination greater than 12, the light blue atoms represent a coordination of 12 other than fcc, and the dark blue atoms represent a coordination less than 12. The contour for the Si atoms colored according to the CNA/CN characterization is as follows: the purple atoms represent the tetrahedral bonding in the diamond cubic lattice, the white atoms represent coordination greater than 4, and the dark blue atoms

represent a coordination of less than 4. The time step for all of the MD simulation runs was chosen to be 4 fs. The temperature was allowed to evolve during the deformation process.

5.1 Strengthening Behavior of the Al/Si Nanocrystalline Composite

At the macro scale, the strengths of materials are typically analyzed using the commonly used phenomenological yield criteria such as von Mises and Tresca [Hertzberg, 1996]. While, these criteria have been found to be appropriate to study deformation behavior in metals under quasi-static loading conditions, recent MD simulations suggest that several effects result in asymmetries in the tensile and compressive strengths and render these criteria to be inappropriate under dynamic loading conditions [Dongare et al., 2010a; Dongare et al., 2010b]. As a result, the. MD simulations of uniaxial stress loading were carried out to compute the flow stress of the composite at high strain rates. Deformation simulations were carried out at constant strain rate by deforming the sample in the loading direction while maintaining zero stress conditions in the lateral directions. The scaling parameter in the loading directions is chosen so as to achieve a strain rate of 10^9 s^{-1}. For each nanocrystalline system, three deformation simulations are carried out independently for loading in the X, Y, and Z directions to eliminate the effect of loading direction on the orientation of the Si grains in the composite.

Si Grains	Flow Stress (GPa) in (Tension/Compression)			
(wt. %)	σ_f^x	σ_f^y	σ_f^z	σ_f^{av}
0.00	1.750/1.835	1.689/1.846	1.694/1.536	1.711/1.739
4.65	1.665/1.851	1.718/1.901	1.737/1.859	1.707/1.870
16.28	1.493/1.738	1.572/1.741	1.530/1.785	1.532/1.755
27.91	1.848/2.166	2.113/2.294	1.926/2.258	1.962/2.239
34.88	1.801/2.173	1.896/2.211	1.812/2.139	1.836/2.174
39.53	2.049/2.411	2.171/2.456	2.042/2.451	2.087/2.439

Table 1. Calculated values of flow (peak) stress during uniaxial tensile/compressive deformation of nanocrystalline Al/Si composites with an average grain size of 6 nm and varying Si volume fraction at a constant strain rate of 10^9 s^{-1}.

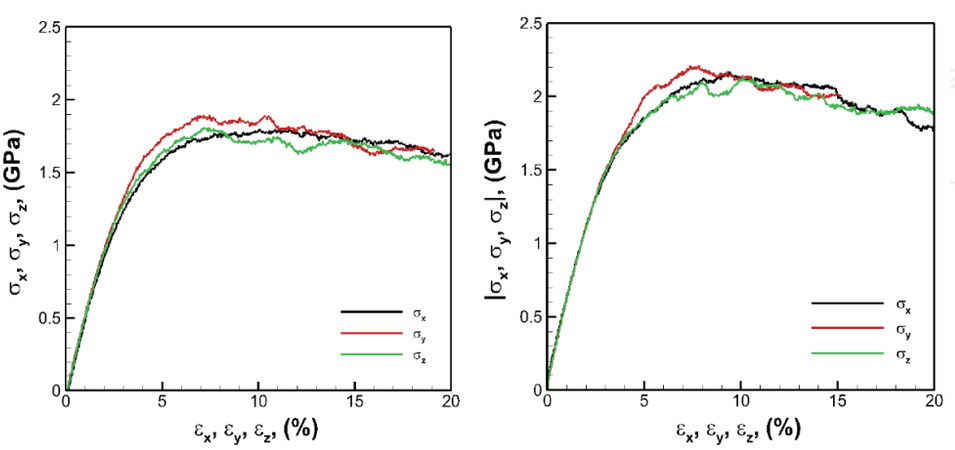

(a) (b)

Fig. 3. Stress-strain curves for deformation of nanocrystalline Al/Si sample containing ~ 35 % Si grains under loading conditions of (a) uniaxial tensile stress, and (b) uniaxial compressive stress. The three curves represent the deformation in X, Y and Z directions. Here εx, εy, and εz are the engineering strains in the X, Y, and Z directions, respectively.

The stress-strain curves obtained for the composite with a volume fraction of ~ 35 % Si are plotted in Fig. 3.(a) and (b) for loading in tension and compression, respectively. The curves are initially linear and lie on top of each other up to the yield point, after which they start to deviate from elastic behavior. The flow stress (σf) is defined as the peak value of the stress in the stress-strain curve [Dongare et al., 2010b; Dongare et al., 2010c]. It can be seen from Fig. 3. that the nanocrystalline composite is stronger in compression than in tension. The flow stress for the nanocrystalline Al/Si composite for various compositions are tabulated in Table 1 for conditions of uniaxial tensile stress and uniaxial compressive stress loading at a constant strain rate of 10^9 s^{-1}.

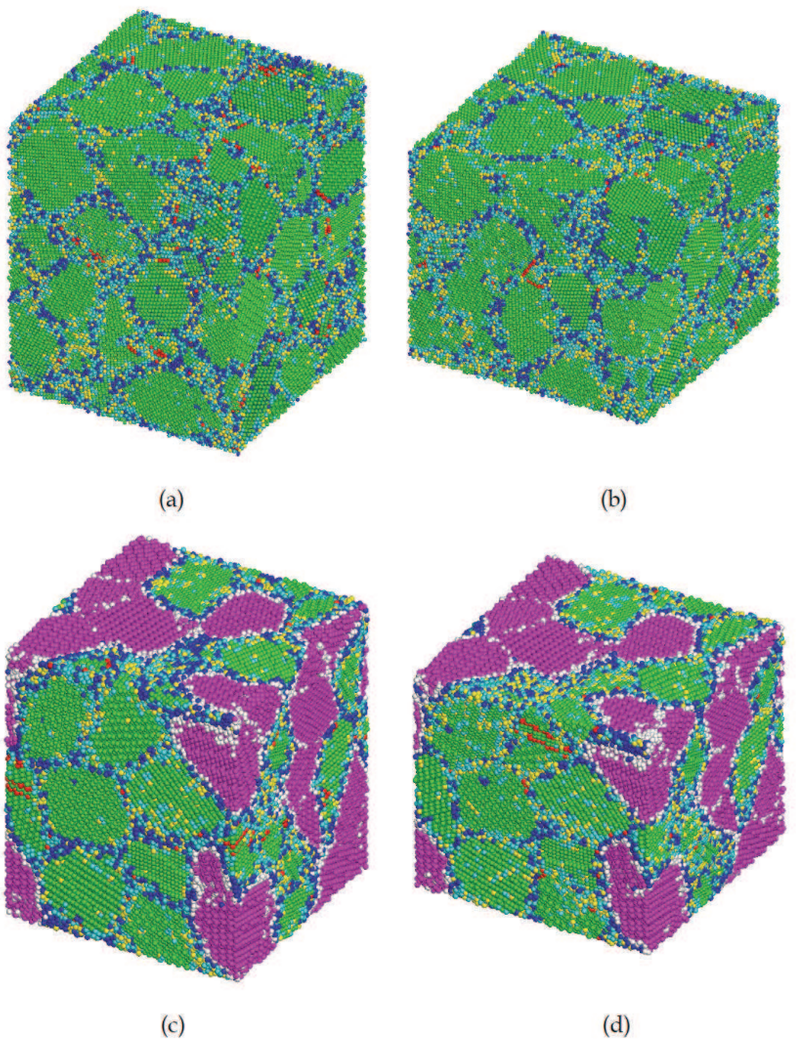

Fig. 4. Snapshots of the nanocrystalline Al system at a strain of 10 % in (a) tensile loading and (b) Compressive loading. The nanocrystalline Al/Si system with a volume fraction of ~40% Si at the same strain are shown in (c) for tensile loading, and in (d) for compressive loading. The atoms are colored according to the CNA/CN contour as indicated in Fig. 2

The snapshots for the nanocrystalline Al system at 10% strain are shown in Fig. 4.(a) for conditions of tensile loading and in Fig. 4.(b) for conditions of compressive loading at a strain of 10 %. Intermediate snapshots of composite containing ~ 35 % Si grains are shown in Fig. 4.(c) for conditions of tensile loading and in Fig. 4.(d) for conditions of compressive loading at a strain of 10 % with the atoms colored according to the CNA/CN characterization. The

snapshots do not show significant dislocation activity in the nanocrystalline Al and the Al/Si composite due to the small grain size (6 nm) of the nanocrystalline systems. While no dislocations are observed in the Si grains, it can be seen that the presence of the reinforcing phase does not significantly alter the dislocation density of the Al grains. The higher strengths in the composite are therefore attributed to reduced grain boundary rotation/sliding at the Al/Si grain boundaries. The fraction of Al/Si grain boundaries increases with increasing fractions of Si grains and therefore results in higher strength of the nanocrystalline composite.

The average values of the flow stress in tension and compression are plotted in Fig. 5.(a) as a function of Si composition. While there are some deviations, the plot shows a general trend that the flow stress values increase with increasing Si fraction. The deviations in the trend are attributed to the small system size and the small number of grains. The asymmetry in the strength of the nanocomposites in tension and compression is plotted in Fig. 5.(b) for various Si compositions. The strength asymmetry for the pure nanocrystalline Al system is predicted to be very small (~ 1.6 %) and addition of Si results in an increase in the asymmetry as the Si composition in the nanocomposites increases. The higher asymmetry in the strength values at higher volume fractions results from the limited grain boundary rotation/sliding behavior of the Al/Si grain boundaries in compression as compared to tension as observed for pure nanocrystalline systems at higher strain rates [Dongare et al., 2010b; Dongare et al., 2010c]. These results are consistent with results from MD simulations using the MEAM potential which suggest that the inclusion of Si particles reduces the relative motion of the Al grains by suppressing both sliding/shearing along the grain boundaries and dislocation nucleation from the boundaries that results in enhanced strengths of the Al–Si nanocomposites [Ward et al., 2006].

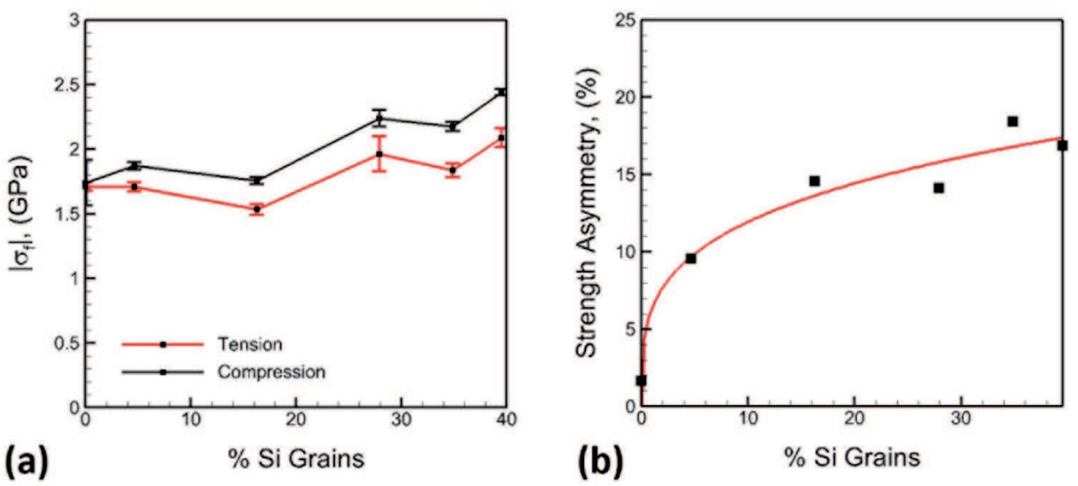

Fig. 5. (a) Calculated flow stress curves for deformation of nanocrystalline Al/Si sample for various volume fractions of Si. The red colored curve corresponds to tensile loading conditions and the black curve corresponds to compressive loading conditions.

5.2 Failure Behavior of the Al/Si Nanocrystalline Composite

The failure behavior of nanocomposites formed by adding Si particles to Al nanocrystalline materials has been investigated using molecular dynamics simulations with the MEAM potential [Ward et al., 2006]. These results suggest that failure initiates by the nucleation of a void at the interface between the Al/Si grains. Experimental studies of deformation and fail-

ure of the A359 alloy at high strain rates also suggest that the fracture propagates along the interdendritic network of Si [Li et al, 2007]. A valid test of the A-EAM potential, therefore, is to study the micromechanisms related to ductile failure in nanocrystalline Al/Si composites consisting of an embedded Si nanocrystal in a nanocrystalline Al matrix. Deformation is carried out under conditions of uniaxial expansion ($\varepsilon_x = \varepsilon_y = 0$, and $\varepsilon_z = \varepsilon$) at a constant strain rate of 109 s-1 to relate to experimental dynamic loading conditions of dynamic failure [Dongare et al., 2009c]. Three deformation simulations are carried out independently for loading in the X, Y, and Z directions to eliminate the effect of loading direction on the orientation of the Si grains in the composite.

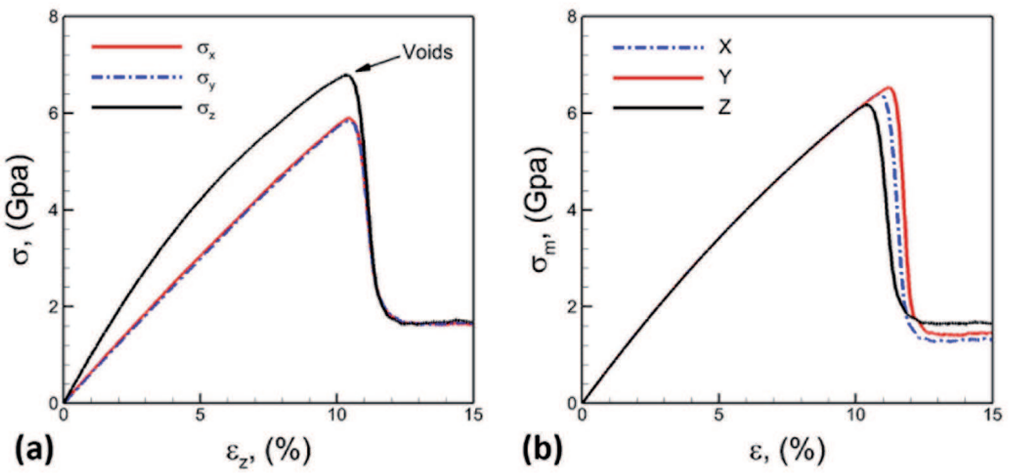

Fig. 6. (a) Plots of stresses in X, Y, and Z direction as a function of strain (εz) during tensile deformation under conditions of uniaxial strain at a strain rate of 10^9 s^{-1}. (b) Evolution of mean stress σm during uniaxial tensile strain loading independently in the X, Y, and Z directions at a strain rate of 10^9 s^{-1}.

The stresses averaged over the entire system in the X, Y, and Z direction and the are plotted in Fig. 6.(a) as a function of engineering strain (ε) for uniaxial tensile strain loading in the Z direction. The evolution of mean stress (σm) as a function of engineering strain (ε) in the loading direction is plotted in Fig. 6.(b) as obtained in the three simulation runs during uniaxial tensile strain loading independently in the X, Y, and Z directions. The stress-strain curves in Fig. 6 show three stages of deformation. The first stage corresponds to elastic deformation of the nanocrystalline system leading to a linear evolution of the curves for σ_x, σ_y, and σ_z up to the yield point. Continued deformation results in deviation from linearity due to GB sliding/rotation processes that are accommodated by the nucleation of dislocations [Dongare et al., 2009c]. Continued deformation results in an increase in the stress to a peak value after which, nucleation of voids results in the relaxation of stresses as indicated by a sharp drop in the stresses in the X, Y, and Z directions as shown in Fig. 6.(a). The stress state transitions to an almost hydrostatic stress condition $(\sigma_x \sim \sigma_y \sim \sigma_z)$, resulting in a sharp drop in the stress values and mean stress values until a minimum is reached. Continued deformation results in the stress state to transition back to that corresponding to uniaxial strain.

Intermediate snapshots of a section of the system are illustrated in Fig. 7. with the atoms colored according to CAN/CN contour. The snapshot in Fig. 7.(a) corresponds to a time just before the peak in the stress value (ε ~ 9.0 %). A single void is observed to nucleate at a grain

boundary interface between the embedded Si nanocrystal and the neighboring Al grains in Fig. 7.(b). Also, there is relatively little dislocation activity at the GB interface between the Al/Si grains. This indicates that void nucleation cannot be attributed to a dislocation pile-up process, but rather results from the mechanical separation/sliding at the Al/Si grain boundary interface. The creation of the void is accommodated by the shearing of the nearby atoms leading to the formation of a disordered shell of atoms around the void as shown in Fig. 7.(c). Continued deformation increases the size of this shell of disordered atoms around the voids and the void shape changes to near spherical as shown in Fig. 7.(b)-(d). Although a few dislocations are observed to propagate into the grains surrounding the void, most of the material surrounding the void consists of disordered atoms and void growth is observed to occur by the shearing of the disordered regions. The creation of disordered atoms surrounding the void increases until a minima in stresses is reached in Fig. 6. This minima in stresses corresponds to the snapshot shown in Fig. 7.(e). A transition in the stress state back to that corresponding to uniaxial strain conditions results in a slower growth rate of the void that is accompanied by the recrystallization of the surrounding disordered regions. The recrystallization of the disordered region around the void is attributed to the increased temperature of the system due to nucleation and growth of the void [Dongare et al, 2009c]. The results from these MD simulations thus agree with those predicted by the MEAM potential [Ward et al, 2006] that the failure of the nanocomposite is initiated by the nucleation of the void at the Al/Si interface.

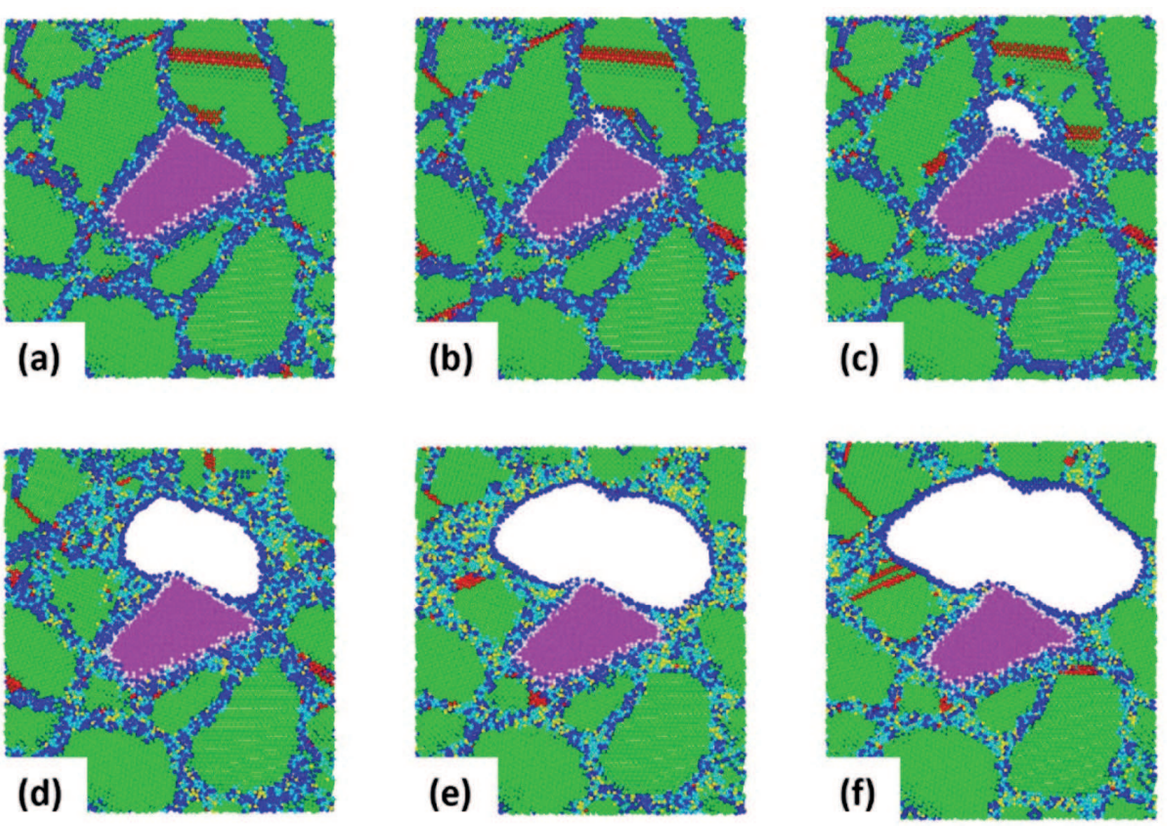

Fig. 7. Snapshots of a section of the system at (a) 90 ps (ε_z ~ 0.09), (b) 100 ps (ε_z ~ 0.10), (c) 105 ps (ε_z ~ 0.105), (d) 110 ps (ε_z ~ 0.11), (e) 120 ps (ε_z ~ 0.12), and (d) 150 ps (ε_z ~ 0.15), showing the nucleation and growth of the void under conditions of uniaxial tensile strain at a constant strain rate of 10^9 s^{-1}. The atoms are colored according to CNA/CN contour.

The value of the maximum mean tensile stress in Fig. 6.(b) can be compared to the peak spall pressure during spallation experiments. The plots suggest that the spall strength changes slightly for the nanocrystalline Al/Si composite with a change in loading direction. Intermediate snapshots of a section of the system at a strain of ε = 11 % during loading under conditions of uniaxial tensile strain in the X direction, the Y direction, and the Z direction are shown in Fig. 8.(a), (b), and (c), respectively at a constant strain rate of 109 s-1. The snapshots suggest that failure (nucleation of void) initiates along the Al/Si grain boundary interface. Thus, the embedding of a Si nanocrystal results in the initiation of failure at the Al/Si interface irrespective of the loading conditions. These results suggest that the failure resistance behavior of these metal-matrix composites is dependent on the characteristics of the metal-ceramic interfaces in the nanocomposites. More work is needed to be done to obtain the links between the length scales (particle size/distribution, layer thickness) and properties (structure, chemistry, etc.) of these composites for enabling high strength behavior and improved failure resistance so as to allow for an optimized microstructural design of the MMnCs for use in extreme environments.

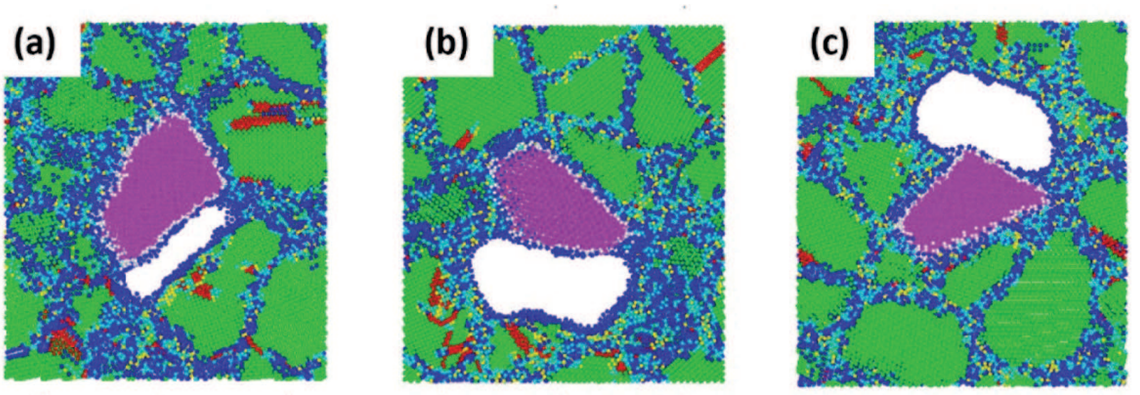

Fig. 8. Sectional snapshots of the nanocrystalline Al/Si system showing initiation of failure along the Al/Si grain boundary interface at a strain of ε = 11 % during loading under conditions of uniaxial tensile strain in (a) X direction (εz = εy = 0, and εx = ε), (c) Y direction (εx = εz = 0, and εy = ε), and (a) Z direction (εx = εy = 0, and εz = ε), at a constant strain rate of 109 s-1. The atoms are colored according to CNA/CN contour.

6. Conclusion

A new angular-dependent EAM interatomic potential is developed that allows for the study of metal-ceramic interfaces at the atomic scale. The A-EAM potential is obtained by combining the EAM potential for Al with the SW potential for Si. The A-EAM potential retains the original functional forms and parameters and therefore all the properties of the pure components as predicted by the original SW and EAM potentials. The formulation of the A-EAM potential limits the parameterization to only the cross-interaction between the Al-Si components. An example parameterization is demonstrated for the Al/Si system based on the on the results of DFT calculations performed for artificial bulk Al/Si alloys and the compositional dependence of the enthalpy of mixing in liquid Al-Si alloys at 1870 K. Large scale molecular dynamics simulations using the A-EAM potential are carried out to study the strengthening behavior of the ceramic (Si) particle reinforced nanocrystalline metal (Al) matrix composites for varying volume fractions of the ceramic phase. The results suggest that the strength of the nanocrystalline composite increases with an increase in the volume frac-

tion of the ceramic phase. The nanocrystalline composite is observed to be stronger in compression loading as compared to tensile loading and this strength asymmetry is observed to increase with increasing volume fraction of the ceramic phase. The microscopic mechanisms related dynamic failure predicted using MD simulations suggest that failure initiates at the metal-ceramic interface. These results suggest that the performance of the nanocomposites in extreme environments can be improved by a tailored design of a metal-ceramic interfaces in the nanocomposite. Future work will therefore focus on a fundamental understanding of the effect of the structure, size and distribution of the reinforcing ceramic phase that will enable high strengths of the nanocomposite in extreme environments.

7. Acknowledgment

This work has been done during AMD's tenure as a National Research Council (NRC) Research Associate funded by the US Army Research Office.

8. References

Albe K., Nordlund K., and Averback R. S. (2002). Modeling the metal-semiconductor interaction: Analytical bond-order potential for platinum-carbon. *Phys. Rev. B*, Vol. 65, No. 19, pp. 195124 , ISSN: 1098-0121

Allen M. P., Tildesley D. J. (1987). *Computer simulation of liquids*, Clarendon Press, ISBN: 0198556454, Oxford

Baskes M.I. (1992). Modified embedded-atom potentials for cubic materials and impurities. *Phys Rev B*; Vol. 46, No. 5, pp. 2727-2742, ISSN: 0163-1829

Brenner D. W. (1989). Relationship between the embedded-atom method and Tersoff potentials. *Phys. Rev. Lett.*, Vol. 63, No. 9, pp. 1022-1022, ISSN: 0031-9007

Brenner D. W. (1990). Empirical potential for hydrocarbons for use in simulating the chemical vapor deposition of diamond films. *Phys. Rev. B*, Vol. 42, No. 15, pp. 9458-9471, ISSN: 0163-1829

Daw M. S. and Baskes M. I. (1984). Embedded-atom method: Derivation and application to impurities, surfaces, and other defects in metals. *Phys. Rev. B*, Vol. 29, No. 12, pp. 6443-6453, ISSN: 1098-0121

Derlet P. M. and Van Swygenhoven H. (2003). Atomic positional disorder in fcc metal nanocrystalline grain boundaries. *Phys. Rev. B*, Vol. 67, No. 1, pp. 014202, ISSN: 1098-0121

Ding K. and Andersen H. (1986). Molecular-dynamics simulation of amorphous germanium. Phys. Rev. B, Vol. 34, No. 10, pp. 6987-6991, ISSN: 0163-1829

Dongare A. M., Neurock M., and Zhigilei L. V. (2009). Angular-dependent embedded atom method potential for atomistic simulations of metal-covalent systems. *Phys. Rev. B*. 80, No. 18, pp. 184106, ISSN: 1098-0121

Dongare A. M., Zhigilei L. V., Rajendran A. M., and LaMattina B. (2009). Atomic scale modeling of multi-component interactions in nanocomposites, *Compos. Part B - Eng.*, Vol. 40, No. 6, pp. 461-467, ISSN: 1359-8368

Dongare A. M., Rajendran A. M., LaMattina B., Zikry M. A., and Brenner D. W. (2009). Atomic scale simulations of ductile failure micromechanisms in nanocrystalline Cu at high strain rates. *Phys. Rev. B*, Vol. 80, No. 10, pp. 104108, ISSN: 1098-0121

Dongare A. M., Rajendran A. M., LaMattina B., Zikry M. A., and Brenner D. W. (2010). Atomic scale study of plastic-yield criterion in nanocrystalline metals using molecular dynamics simulations. *Metall. Mater. Trans. A*, Vol. 41A, No. 2, pp. 523 - 531, ISSN: 1073-5623

Dongare A. M., Rajendran A. M., LaMattina B., Zikry M. A., and Brenner D. W. (2010). Tension-Compression Asymmetry in Nanocrystalline Cu: High Strain Rate vs Quasi-Static Deformation. *Comp. Matl. Sci.*, Vol. 49, No. 2, pp. 260 -265, ISSN: 0927-0256

Dongare A.M., Rajendran A. M., LaMattina B., Zikry M. A., and Brenner D. W. (2010). Atomic scale studies of spall behavior in nanocrystalline Cu. *J. Appl. Phys.*, Vol. 108, No. 11, pp. 113518, ISSN: 0021-8979

Dongare A.M., Irving D. L., Rajendran A. M., LaMattina B., Zikry M. A., and Brenner D. W. (2011). Physical Rev. B, In review.

Foiles S. M. (1985). Application of the embedded-atom method to liquid transition metals. *Phys. Rev. B*, Vol. 32, No. 32, pp. 3409-3415, ISSN: 0163-1829

Germann TC, Kadau, K (2008). Trillion-atom molecular dynamics becomes a reality. *Int. J. Mod. Phys. C*, Vol. 19, No. 9, pp. 1315-1319, ISSN: 0129-1831

Hertzberg R. W. (1996). *Deformation and fracture mechanics of engineering materials*, 4th ed., Wiley, ISBN: 0471012149, New York (NY), USA

Honneycutt D. J. and Andersen H. C. (1987). Molecular dynamics study of melting and freezing of small Lennard-Jones clusters. *J. Phys. Chem.*, Vol. 91, No. 19, pp. 4950-4963, ISSN: 0022-3654

Johnson R. A. (1988). Analytic nearest-neighbor model for fcc metals. *Phys. Rev. B*, Vol. 37, No. 37, pp. 3924-3931, ISSN: 0163-1829

Kanibolotsky D. S., Bieloborodova O. A., Kotova N. V. and Lisnyak V. V. (2002). Thermodynamic properties of liquid Al-Si and Al-Cu alloys. *J. Therm. Anal. Calorim.*, Vol. 70, No. 3, pp. 975-983, ISSN: 1418-2874

Li Y., and Ramesh K. T. (1998). Influence of particle volume fraction, shape, and aspect ratio on the behavior of particle-reinforced metal–matrix composites at high rates of strain. *Acta Mater.*, Vol. 46, No. 6, pp. 5633-5646, ISSN: 1359-6454

Li Y., Ramesh K. T., Chin E. S. C. (2007). Plastic Deformation and failure in A359 aluminum and an A359-SiCp MMC under quasistatic and high-strain-rate tension. *J of Compos Mater.*, Vol. 41, No. 1, pp. 27-40, ISSN: 0021-9983.

Mishin Y., Farkas D., Mehl M. J., and Papaconstantopoulos D. A. (1999). Interatomic potentials for monoatomic metals from experimental data and ab initio calculations. *Phys. Rev. B*, Vol. 59, No. 5, pp. 3393-3407, ISSN: 1098-0121

Mortensen A., and Suresh S. (1995). Functionally graded metals and metal-ceramic composites: Part 1 Processing. *Int. Mat. Rev.*,Vol. 40, No. 6, pp. 239-265, ISSN: 0950-6608.

Nakayama T., Itaya S., and Murayama D. (2006). Nano-scale view of atom intermixing at metal/semiconductor interfaces. *J. Phys.: Conf. Ser: 7th International Conference on New Phenomena in Mesoscopic Structures/5th International Conference on Surfaces and Interfaces of Mesoscopic Devices*, Vol. 38, pp. 216-219, Maui, HI, Nov 27-Dec 02, 2005, ISSN: 1742-6588

Remington B. A., Bazan G., Belak J., Bringa E., Caturla M., Colvin J. D., Edwards M. J., Glendinning S. G., Ivanov D. S., Kad B., Kalantar D. H., Kumar M., Lasinski B. F., Lorenz K. T., McNaney J. M., Meyerhofer D. D., Meyers M. A., Pollaine S. M., Rowley D., Schneider M., Stölken J. S., Wark J. S., Weber S. V., Wolfer W. G., Yaakobi B., and Zhigilei L. V. (2004). Materials science under extreme conditions of pressure and strain rate. *Metall. Mater. Trans. A* Vol. 35, No. 9, pp. 2587-2607, ISSN: 1073-5623

Stillinger F. H. and Weber T. A. (1985). Computer simulation of local order in condensed phases of silicon. *Phys. Rev. B* 31 5262-5271, ISSN: 0163-1829

Suresh S., and Mortensen A. (1997). Functional graded metals and metal-ceramic composites: Part 2 Thermomechanical Behavior. *Int. Mat. Rev.*, Vol. 42, No. 3, pp. 85-116, ISSN: 0950-6608

Tersoff J. (1988). New empirical approach for the structure and energy of covalent systems. *Phys. Rev. B*, Vol. 37, No. 12, pp. 6991-7000, ISSN: 0163-1829

Tersoff J. (1988). Empirical interatomic potential for carbon, with applications to amorphous carbon. *Phys. Rev. Lett.*, Vol. 61, No. 25, pp. 2879-2882 , ISSN: 0031-9007

Thijsse B.J. (2005). Silicon potentials under (ion) attack: Towards a new MEAM model. *Nucl Instrum Meth B*; Vol. 228, Sp. Iss. SI, pp. 198-211, ISSN: 0168-583X

Thijsse B. J. (2002). Relationship between the modified embedded-atom method and Stillinger-Weber potentials in calculating the structure of silicon. *Phys. Rev. B*, Vol. 65, No. 19, pp. 195207, ISSN: 1098-0121

Ward D.K., Curtin W.A. and Qi Y. (2006), Mechanical behavior of aluminum–silicon nanocomposites: A molecular dynamics study. *Acta Mater.*, Vol.54, No. 17, pp. 4441-4451, ISSN: 1359-6454